

# Crystal anisotropy implications on the intrinsic magnetic and optical properties in van der Waals FePS<sub>3</sub>

Ellenor Geraffy<sup>1#</sup>, Shahar Zuri<sup>1#</sup>, Milosz Marcin Rybak<sup>2</sup>, Faris Horani<sup>1</sup>, Adam K. Budniak<sup>1</sup>, Yaron Amouyal<sup>3</sup>, Magdalena Birowska<sup>\*2</sup> and Efrat Lifshitz<sup>\*1</sup>

<sup>1</sup>Schulich Faculty of Chemistry, Solid State Institute, Russell Berrie Nanotechnology Institute, and the Helen Diller Quantum Information Center, Technion – Israel Institute of Technology, 3200003 Haifa, Israel

<sup>2</sup>Institute of Theoretical Physics, Faculty of Physics, University of Warsaw, Pasteura 5, Warsaw 02-093, Poland

<sup>3</sup>Department of Materials Science and Engineering, Technion – Israel Institute of Technology, 3200003 Haifa, Israel

#Equal contribution

\*Corresponding authors

Email: [ssefrat@technion.ac.il](mailto:ssefrat@technion.ac.il) , [birowska@fuw.edu.pl](mailto:birowska@fuw.edu.pl)

Keywords: 2D materials, semiconductors, magneto-optics, anti-ferromagnetism.

Antiferromagnetic (AFM) FePS<sub>3</sub> has gained significant interest recently for its potential applications in spin-related devices. A single layer is comprised of a honeycomb network, stabilized by long-range spin-exchange interactions, with a *zigzag* or *Neél* arrangement of the Fe-atoms. This study exposed, for the first time, a strong impact of lateral crystal distortion on the magnetic arrangement and optical properties of FePS<sub>3</sub>. This impact was deciphered by correlating photoluminescence (PL) observations with single-crystal XRD which uncovered anisotropy in the a/b crystallographic plane. Thus, inducing a breakage in the inversion symmetry in FePS<sub>3</sub> causing changes in its electronic and optical transitions. The MPL observations exhibited an unexpected band-edge circularly polarized recombination emission, while off-band-edge transitions were linearly polarized. Also, temperature-dependent MPL measurements reflected *zigzag*-AFM at low temperatures and the coexistence of *zigzag* or *Neél* at mid temperatures. Theoretical calculation implementing anisotropy in spin-exchange interactions among Fe atom's nearest neighbors revealed stabilized *zigzag* arrangement tilted away from the a-axis. Furthermore, DFT calculations of the electronic band-edge predicted split states in degenerate symmetric points (K+/K-) for *zigzag* structure and non-degenerate for the *Neél* arrangement. Highlighting the importance of the inclusion of a crystallographic anisotropy parameter for the simulation of the experimental observations.

## 1. Introduction

The interest in two-dimensional (2D) van der Waals (vdW) materials has grown immensely in recent years due to their potential applications in spin-electronic and spin-optical devices.<sup>1,2</sup> Magnetic vdW materials, such as CrI<sub>3</sub>, Cr<sub>2</sub>Ge<sub>2</sub>Te<sub>6</sub>, and Fe<sub>3</sub>GeTe<sub>2</sub>, raised interest recently for their dominant ferromagnetic (FM) configuration down to the monolayer limit, spin-Hall effect, and magnetic Kerr rotation.<sup>3–5</sup> Recently, renewed attention has been given to *transition metal trichalcogenides* (MPX<sub>3</sub>; M = first-row transition metal; X = chalcogenide) for their predominant anti-ferromagnetism (AFM) and semiconductor properties.<sup>6–8</sup> A single layer of MPX<sub>3</sub> is composed of covalently bonded FeS<sub>6</sub> octahedra and [P<sub>2</sub>S<sub>6</sub>]<sup>4-</sup> bipyramids at a ratio of 2:1. The metals form a hexagonal honeycomb arrangement, with P-P pairs positioned at the hexagons' center (see **Figure 1**). The adjacent layers are held together along the c-crystallographic axis by weak vdW interactions, thus enabling the exfoliation of bulk crystals down to a few- or single-layer.<sup>9–11</sup> The unpaired spins in the d-orbitals of the metal cations, along with their honeycomb arrangement in the MPX<sub>3</sub> single-layer enable exchange interactions among nearest neighbor spins (NNs) to form a long-range AFM order. This claim is in contradiction to the Mermin-Wagner-Hohenberg theorem which states that long-range magnetism cannot exist at finite temperatures.<sup>12,13</sup> However, due to the spatial and electronic confinement of MPX<sub>3</sub> materials, as well as a structural anisotropy within single layers, this becomes possible. Thus, the intrinsic magnetism of the MPX<sub>3</sub> compounds makes them most suitable for the study of AFM properties at a nearly atomistic limit with a perspective for application in new opto-spintronic devices and catalysis applications.<sup>6,9,14–16</sup>

The magnetic ordering of MPX<sub>3</sub> compounds can be regulated by an exchange of the metal cations, i.e. MnPS<sub>3</sub>,<sup>17–20</sup> FePS<sub>3</sub>,<sup>21–24</sup> and NiPS<sub>3</sub>,<sup>25,26</sup> all possess varying Neél-AFM (N-AFM) or zigzag-AFM (z-AFM) configurations,<sup>8,27–31</sup> that can be further manipulated by external stimuli such as temperature and magnetic field.<sup>6</sup> N-AFM configurations consist of NNs metal atoms of opposite orientation while in z-AFM configurations adjacent spin states of metal atom chains along the zigzag direction possess an opposite orientation. The long-range order in these materials is stabilized by spin-exchange interactions among first, second, and third NNs, with substantially weaker interlayer interactions ( $\sim 1/200$ ).<sup>32</sup> Among the MPX<sub>3</sub> family, FePS<sub>3</sub> is a particularly intriguing material due to its z-AFM order with an Ising orientation.<sup>31,33</sup> These characteristics bestow interesting magneto-optical properties, some of which remain unexplored and will be the focus of the current study.

Bulk FePS<sub>3</sub> possesses a monoclinic unit cell with the space group C2/m with z-AFM magnetism. The a/b plane includes FM-coupled metal atoms along a *zigzag* chain, where adjacent chains have an AFM relation up to the Neél temperature ( $T_N \sim 120$ K); beyond this, spin frustration and a transition into a paramagnetic configuration occurs.<sup>23,34,35</sup> A recent temperature-dependent magnetic susceptibility study revealed a positive Weiss FM constant ( $\theta = 16$ K) for the Fe-*zigzag* chains.<sup>14,27</sup> Furthermore, Chittari *et al.*<sup>8</sup> and Mayorga-Martinez *et al.*<sup>14</sup> commented that Fe<sup>2+</sup> (possessing a d<sup>6</sup> electronic configuration) experiences a spin-orbit coupling, that bestows the material with trigonally distorted FeS<sub>6</sub> octahedra and a weak crystallographic anisotropy.<sup>8,14</sup> **Figure 1** shows a comparison of an isotropic MnS<sub>6</sub> octahedra and distorted FeS<sub>6</sub> octahedra whereby the Fe-S bonds are not equivalent. Moreover, previous temperature-dependent X-ray diffraction (XRD) studies report that the a:b lattice constants'

ratio has a strong temperature dependence,<sup>35</sup> and thus may induce a local symmetry breaking in the honeycomb structure with a further adjustment of the NNs' distances. Such lateral distortion may impact the optical properties along with the creation of a magnetic phase transition, i.e., z-AFM to a full FM (owing to their close energetic proximities).<sup>8,14,36</sup> Moreover, a recent study proposed that the z-AFM arrangement induces a high degree of optical linear dichroism (LD) along the zigzag direction.<sup>21</sup> The axis orientation is a matter of debate with some proposing a zigzag alignment along the a-crystallographic axis,<sup>21</sup> whereas others determined an orientation within the a/b plane.<sup>37,38</sup>

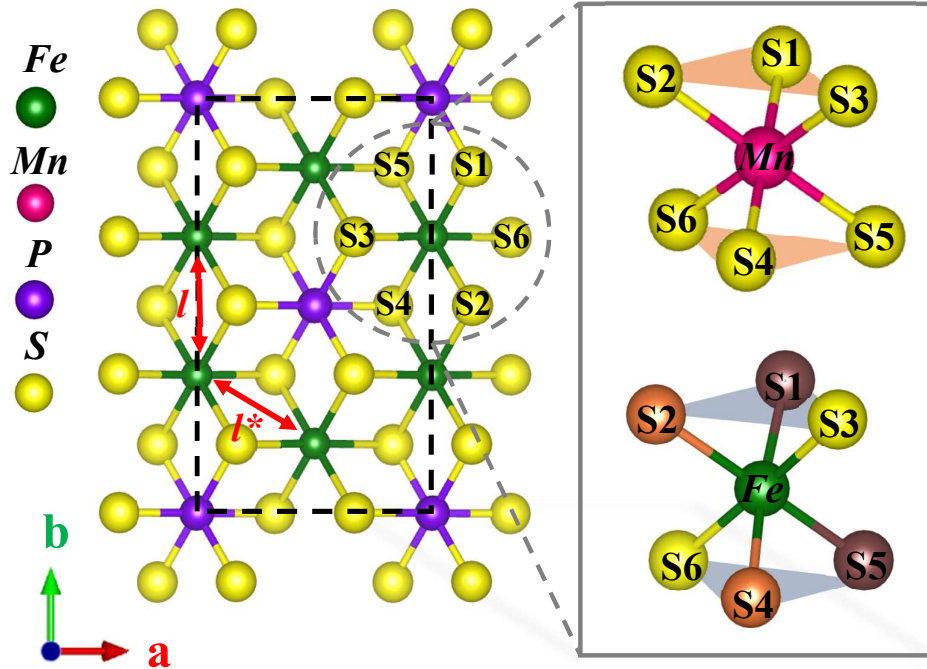


**Figure 1: Crystallographic structure of MPX<sub>3</sub> materials.** Crystal lattice representation of MPX<sub>3</sub> materials, with a close up of an isotropic MnS<sub>6</sub> octahedra and anisotropic FePS<sub>6</sub> octahedra. Non-equivalent Fe-S bonds are marked by different colors of the S atom, highlighting a local inversion symmetry breaking in FePS<sub>3</sub>. Varied Fe-Fe bond lengths are labeled by  $l$  and  $l^*$ .

The current work addresses an open question about the influence of intralayer structural anisotropies on the magneto-optical properties of single crystal FePS<sub>3</sub>. The study included monitoring photoluminescence under the influence of an external magnetic field, with linear and circular optical detection and variable temperature. The work exposed unique optical transitions, one close to band-edge energy with distinguished circular polarization and others at higher energies with linear polarization. Furthermore, XRD measurements showed a large a/b lattice constant ratio. Theoretical electronic band-structure calculations unveiled a band split in a single K- Brillouin point as a consequence of strong spin-orbit coupling, inversion symmetry breaking, and lateral crystal anisotropy. This was corroborated experimentally, with a circularly polarized optical transition and a PL peak splitting above certain temperatures. Furthermore, NNs spin exchange interactions were evaluated by implementing a modified Heisenberg Hamiltonian which includes uneven M-S bond lengths in correlation with the lateral structural anisotropy. Such an evaluation revealed a z-AFM direction along the a/b plane at low

temperatures, and the co-existence of nearly iso-energetic z-AFM and N-AFM phases  $\sim 40\text{K}$ , whereby both were collaborated with the experimental results.

## 2. Results and Discussion

Single-crystal bulk  $\text{FePS}_3$  was synthesized using the chemical vapor transport (CVT) method. The structural and optical characterization of  $\text{FePS}_3$  was presented in our previous work.<sup>39</sup> The crystal's composition was characterized by an energy-dispersive X-ray (EDX), confirming a 1:1:3 of the Fe/P/S atomic ratio with no impurities, as shown in supplement information [SI], **Figure S1**. Single-crystal X-ray diffraction (XRD) measurements at two different temperatures (140K and 296K) of bulk  $\text{FePS}_3$  exposed a structural anisotropy as seen in SI, **Table S1-S4**. This is expressed through uneven M-S and M-M bond lengths. **Figure 1** shows a scheme representing unevenness in M-S bonds by different S-atoms' colors, and that in M-M bonds by the red arrows (labelled  $l$  and  $l^*$ ).

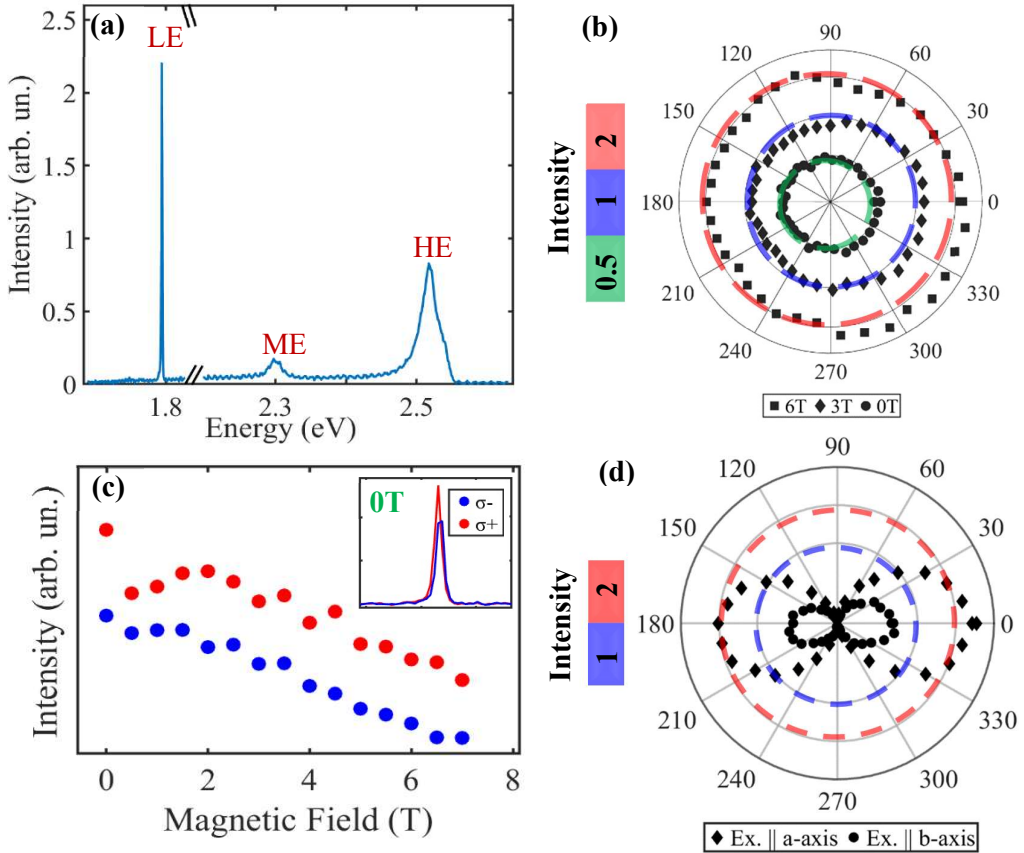


**Figure 2: Optical measurements on bulk  $\text{FePS}_3$ .** (a) Emission spectrum of bulk  $\text{FePS}_3$  at 4K. Three emission peaks are visible; a sharp peak at 1.78eV (LE) and two broader emissions at 2.3eV (ME) and 2.56eV (HE). (b) Polar plot of LE transition band intensities detected with a linear polarizer at magnetic field strengths ranging from 0-6T. (c) Scatter plot of extracted peak intensities of LE transition from gaussian fits of  $\sigma^-$  and  $\sigma^+$  detected circular polarized transitions as a function of magnetic field ranging from 0T-7T. Insert:  $\sigma^-$  and  $\sigma^+$  detected circular polarized plots at 0T. (d) Polar plot of linearly polarized PL of HE transition, excited parallel to the a-axis (diamond) and to the b-axis (circle). Polar plot of linearly polarized PL of HE transition, excited parallel to the a-axis (diamond) and to the b-axis (circle).

The designated anisotropy is expected to grow at lower temperatures. It is further anticipated that the structural anisotropy leads to an inversion symmetry breaking in  $\text{FePS}_3$ , and the consequent impact on the electronic and optical properties of the material, as elaborated in the following section. To reveal the implications of the structural anisotropy in  $\text{FePS}_3$  on the magneto-optical properties of  $\text{FePS}_3$ , various optical measurements were carried out on the single crystal. These include photoluminescence (PL) measurements under the influence of an external magnetic field of various strengths, with opposing circular and linear polarization. In addition, temperature-dependent PL measurements were performed in the range of 4K to 290K. **Figure 2 (a)** displays a PL spectrum of a  $\text{FePS}_3$  single-crystal excited above the band-gap energy (at 3eV) and recorded at 4K. The spectrum is dominated by three distinct emission transitions, centered around: 1.78eV (LE), 2.3eV (ME), and 2.56eV (HE).

**Figure 2 (b)** illustrates a polar plot of the LE emission band's intensity, detected with a linear polarizer at varying magnetic field strengths (see indent). Thus, a lack of linear polarization behavior is detected for the LE transition, in the absence/presence of an external magnetic field. **Figure 2 (c)** displays the LE emission intensities versus field strength under two opposing circular polarization detection ( $\sigma\pm$ ), uncovering a clear circular polarization behavior with dominancy of the  $\sigma^+$  emission. Previous works on  $\text{NiPS}_3$ <sup>25,40</sup> and few-layer/single-layered  $\text{FePS}_3$ <sup>21</sup> have shown the sharp LE band to have a linear polarized behavior. Thus, the unexpected circular polarization observed leaves us with an open question as to why this occurs. This is further corroborated in **Figure 2 (c)** where the circular polarization is shown to exist even at  $B=0$ . This behavior may be attributed to the influence of structural anisotropy of electronic and optical properties, and examination of this reason is extensively elaborated in the theoretical section below. Conversely, the ME and HE transitions exhibit a linear polarization behavior as shown in **Figure 2 (d)**. Recent publications assigned the high-energy bands to d-d transitions,<sup>21</sup> and exposed their linear dichroism (LD), which emanates from a zigzag arrangement along a specific axis. **Figure 2 (d)** shows a polar plot of the linearly polarized PL of the HE transitions, excited along the a-axis (shown in black diamonds) and along the b-axis (shown in black circles). A clear LD dependence is shown along both the a- and b- orientations and thus brings to question the directionality of the zigzag Fe chains within the a/b plane.

Further on, the magnetic stability of z-AFM  $\text{FePS}_3$  was examined by recording the PL spectra at various temperatures. **Figure 3 (a)** depicts a color plot of temperature-dependent measurements at the low energy region (LE). A second band is exposed at  $\sim 10\text{K}$ , appearing blue-shifted from that at 1.78 eV by about 4 meV, labeled here on as LE-1 and LE-2. These bands show a general tendency to low energies at elevated temperatures, having sustained through the entire temperature range. This mutual correlation emanates from a change in the electronic structure as a consequence of a local structural anisotropy, as included in the discussion below. **Figure 3(b)** represents plots of the LE-1's and LE-2's intensities (see Gaussian fits at the SI, **Figure S 4**) versus temperature, possessing a few distinct trends. The intensity of the LE-1 increases while simultaneously that of LE-2 decreases up to 40K, a correlation that may be associated with a competing population distribution between close-by states. Furthermore both curves exhibit a discontinuity  $\sim 120\text{K}$ , which corresponds to the  $T_N$  (indicating an AFM to paramagnetic phase transition). The region between these points refers

to a spin fluctuated metamagnetic status, that gradually increases with the elevation of the temperature. Likewise, **Figure 3(c)** shows a color plot of the temperature-dependent PL of the HE transitions, with the appearance of a second band (HE-1, HE-2) above 10K. In contrast to the LE's transitions, the HE's bands are red-shifted with the increase of temperature, indicating a different nature for the processes at two spectral regimes. **Figure 3(d)** depicts plots of the HE-1's and HE-2's integrated intensities (see Gaussian fits at the SI, **Figure S5**) versus the temperature, exhibiting a sharp decline around 40K that can be correlated with the transition into the metamagnetic phase region while showing a plateau when approaching the  $T_N$ . The metamagnetic phase is linked to the gradual enhancement of the structural anisotropy in  $\text{FePS}_3$ , with a decrease in temperature. This is further supported by our calculations, which revealed a small energy difference (a few meV) between the z-AFM and N-AFM configurations. Previous work of Chittari *et al.*<sup>8</sup> exposed magnetic phase transitions in  $\text{FePS}_3$  triggered by an external strain, resembling the observations discussed here. Beyond, Zhang *et al.*<sup>22</sup> discussed the influence of a strain on the NNs spin exchange and the value of  $T_N$  in  $\text{FePS}_3$ .

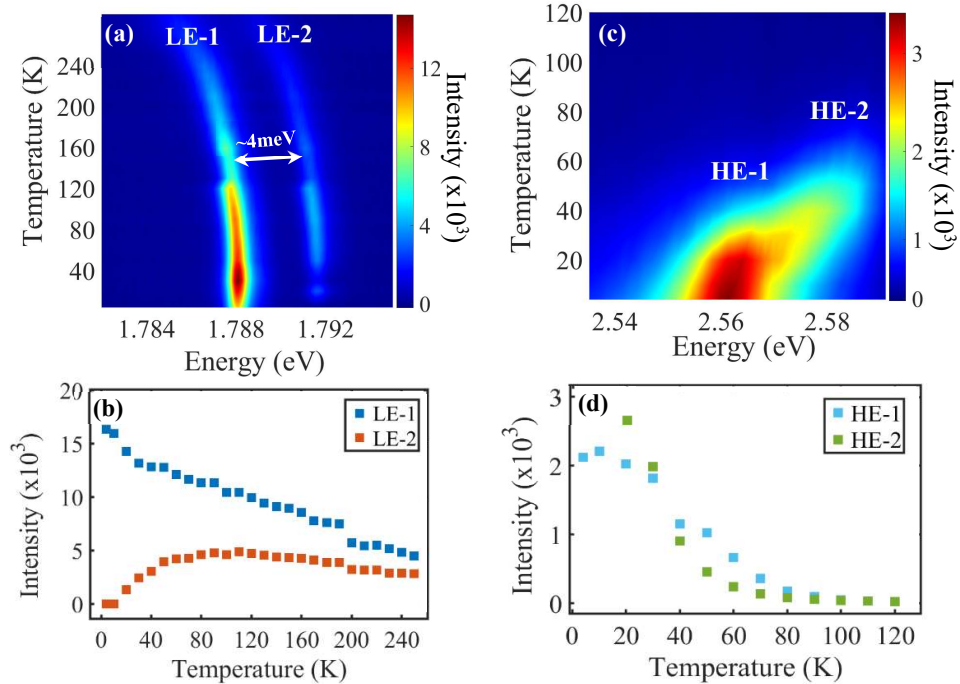


**Figure 3: Temperature dependent PL measurements on bulk  $\text{FePS}_3$ .** (a) Color map of temperature dependent PL ranging from 4K-240K, showing the band separation to be  $\sim 4\text{meV}$ . (b) Scatter plot of peak intensity as a function of temperature of LE transition, extracted from Gaussian fits. (c) Color map of temperature dependent PL ranging from 4K-120K, showing a peak splitting with increase in temperature. (d) Scatter plot of peak intensity as a function of temperature of HE transitions, extracted from Gaussian fits.

The experimental observations discussed above uncovered a few central points: (i) a lateral anisotropy (an increase of the  $b/a$  ratio), pronounced as a distortion of the hexagonal honeycomb structure and a consequence occurrence of inversion-symmetry breaking; (ii) an appearance of double optical transitions at two different spectral regions, each with a selective polarization; (iii) a pronounced relation between magnetic ordering and optical properties. To decipher a correlation among these observations, we evaluated the NNs' spin-exchange

interactions in a distorted honeycomb structure. Additionally, we performed electronic band-structure calculations which included anisotropy in the hexagonal structure, models which enabled the simulation of the optical transitions at specific magnetic configurations. The mentioned theoretical considerations are extensively elaborated here on.

The evaluation of spin exchange interactions was based on the examination of the Fe-S and Fe-Fe bond lengths as in **Table 1**. The indicated distances in the table refer to relaxed atomic positions in the ground state derived via DFT calculations (see **Methods**). **Table 1** exposes three different M-S bonds, also shown schematically in **Figure 1**, compared with MnPS<sub>3</sub>, which acts as a reference to the isotropic honeycomb network. The distortion of the [FeS<sub>6</sub>] octahedra induces unevenness in the Fe-Fe distances.

**Table 1** Anisotropies in atomic distances (MS, MM( $l, l^*$ )) and structural parameters ( $\Delta_b, \delta$ ) for relaxed FePS<sub>3</sub> and MnPS<sub>3</sub>

	a	b	$\delta$	$l$	$l^*$	MS1	MS2	MS3	MS4	MS5	MS6	$\ \Delta_b\ $
	[Å]		[%]									[%]
FePS <sub>3</sub>	6.066	10.526	0.2	3.393	3.563	2.636	2.578	2.572	2.578	2.636	2.572	2.2
MnPS <sub>3</sub>	6.083	10.536	0.0	3.511	3.512	2.624	2.625	2.624	2.625	2.624	2.625	0.0

The anisotropy in FePS<sub>3</sub> is dominated by a change in the b-crystal parameter which is quantified here by a variable,  $\Delta_b$ :

$$\Delta_b = \frac{\text{mean}(MS1, MS5) - \text{mean}(MS2, MS4)}{\text{mean}(MS1-6)} \quad (1)$$

A comparison between the  $\Delta_b$  values in FePS<sub>3</sub> and MnPS<sub>3</sub> (see **Table 1**), reveals unprecedent distortion of the FeS<sub>6</sub> octahedra, and thus conveys a symmetry breaking in the b/a plane. The last is determined by a parameter,  $\delta$ :

$$\delta = (b - a\sqrt{3})/a\sqrt{3} \quad (2)$$

Notably, the magnitude of  $\delta$  is larger by ~0.2% in FePS<sub>3</sub> with respect to that of MnPS<sub>3</sub>. The mentioned intralayer anisotropy also impacts the NNs' spin-exchange interactions. To accommodate for this, the degrees of anisotropy in the spin-exchange couplings were assumed using a Heisenberg Hamiltonian, stated as:

$$H = \sum J_{1,1} \vec{S}_i \cdot \vec{S}_j + \sum J_{1,2} \vec{S}_i \cdot \vec{S}_j + \sum J_{2,1} \vec{S}_i \cdot \vec{S}_j + \sum J_{2,2} \vec{S}_i \cdot \vec{S}_j + \sum J_{3,1} \vec{S}_i \cdot \vec{S}_j + \sum J_{3,2} \vec{S}_i \cdot \vec{S}_j \quad (3)$$

where the NNs exchange interaction coefficients ( $J_{ij}$ ;  $i = 1-3, j = 1, 2$ ) under consideration are marked in **Figure 4(a)**. The magnitudes of  $J_{ij}$  were evaluated from six linear independent equations as given in the **Methods**, using DFT+U energy calculations based on the relaxed M-M distances given in **Table 1**. The  $J_{ij}$  coefficients evaluated for anisotropic FePS<sub>3</sub> are listed in **Table 2** (left column), the average figures over each  $i$  variable and comparison with values of

isotropic  $\text{FePS}_3$  are shown in the middle and right columns, respectively. Interestingly, our calculations showed that isotropic  $\text{FePS}_3$  structure results in a false Neél magnetic ground-state with large deviations from the known exchange interaction terms (see SI, **Table S6**). For isotropic  $\text{FePS}_3$ , significant variance between the exchange terms is obtained, emphasizing the **Error! Reference source not found.** dominance of structural anisotropy over the spin interactions. This implies that even a minor symmetry breaking can cause a meaningful difference in magnetic behavior. The average exchange values are in agreement with those in previous publications with avoided anisotropy.<sup>32</sup> Thus, we conclude that the non-symmetric structure dominates the magnetic behavior of  $\text{FePS}_3$ . Moreover, our results shed light on unexplained neutron inelastic scattering peak broadening that was observed in the past.<sup>22,41,42</sup>

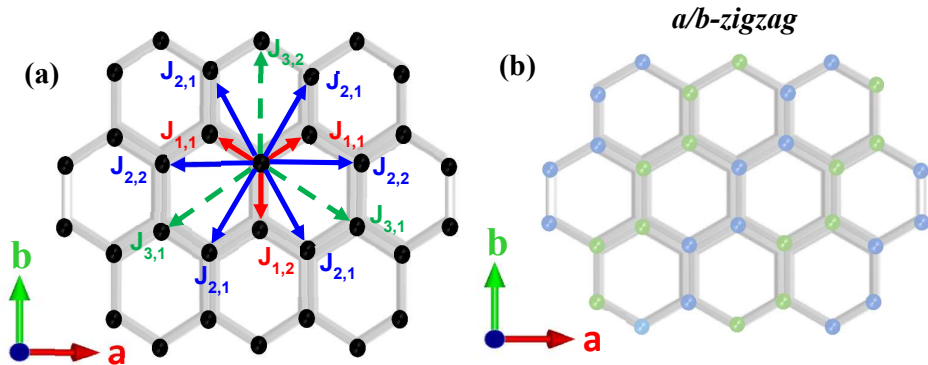


**Figure 4:  $\text{FePS}_3$  magnetic configuration.** (a) A representation of a honeycomb in  $\text{FePS}_3$  with the various nearest-neighbor spin-interactions as in Equation 4. (b) A representation of a honeycomb in  $\text{FePS}_3$  showing the *a/b*-zigzag magnetic configuration, with the most energy favorable configuration as based on the DFT+U calculations.

**Table2 : Comparison between spin-exchange terms in isotropic and anisotropic hexagonal arrangement in  $\text{FePS}_3$**

Anisotropic $\text{FePS}_3$		Average			Isotropic $\text{FePS}_3$	
$J_{11}$ (3.437 Å)	1.42		$J_1$	2.15	$J_1$	0.49
$J_{12}$ (3.467 Å)	3.59					
$J_{21}$ (5.973 Å)	-0.29		$J_2$	-0.28	$J_2$	0.17
$J_{22}$ (5.965 Å)	-0.23					
$J_{31}$ (3.899 Å)	0.27		$J_3$	-1.13	$J_3$	0.07

Furthermore, the DFT calculations unveiled that the *zigzag*-AFM align along *a/b* direction is the stable ground-state magnetic configuration, exceeding the *a*-axis *zigzag* alignment (see SI, **Table S5**). Meaning that the *zigzag* axis does not coincide with the elongation direction of a honeycomb (see **Figure 5(b)**), a situation that was also mentioned in other reports.<sup>37,38</sup> Furthermore, our calculations suggest a competition between the Fe-spin alignment in a *Neél* and *a/b*-*zigzag* configuration, which is in line with a recent report concerning the coexistence of two magnetic phases.<sup>43</sup> Additionally, the *a/b*-*zigzag* magnetic configuration endows the ground-state  $\text{FePS}_3$  with a spin frustration which is chiral in nature. This chirality derives from the mirror symmetry across the *a/c* plane (see the mirror axes,  $J_{i,1}$  in

**Figure 4(a)).** The spin frustration originates from energetically equivalent variations of the *a/b*-zigzag configuration in between the right or left direction. This chirality may intrinsically support spin-waves (magnons) formation in the  $\text{FePS}_3$  system.<sup>42,44,45</sup>

The DFT-based electronic band-structure calculations has been performed within DFT+U ( $U = 5\text{ eV}$ ) approach, including spin-orbit interaction (SOI). The calculation procedures are given in the Methods section. The models are shown schematically in **Figure 5**, and the derived variables for each model are summarized in **Table 3**.

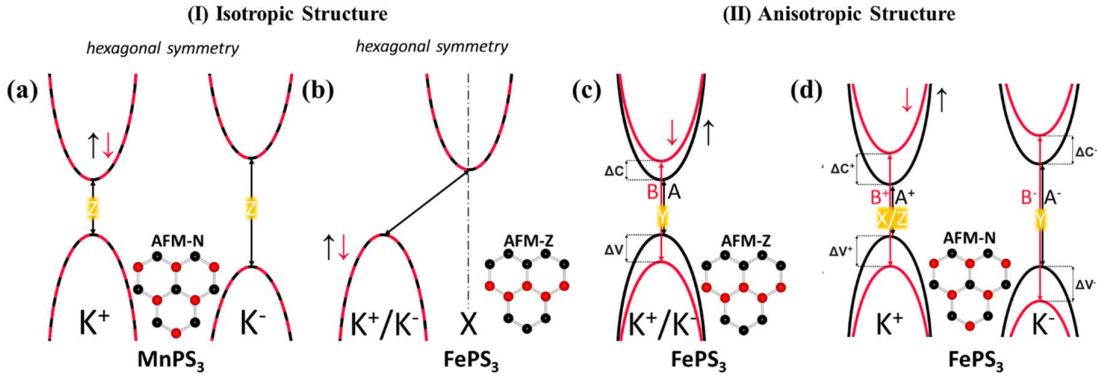


**Figure 5: Schematic band-edge electronic structures of  $\text{MnPS}_3$  and  $\text{FePS}_3$ , based on DFT+U ( $U=5\text{ eV}$ ) calculations for isotropic and anisotropic hexagonal planes (monolayers). The red and black curves and arrows emphasizing states with opposing spin polarities. The double-arrows denote dipole allowed optical transitions, where “z” and “y” designate the emission polarization direction. A and B labels represent spin-conserving transitions.**

**Table 3:** The calculated variables appearing in Figure 5 and in the description of its panels

Str.	Mag. order	$a [A]$ ( $\delta [\%]$ ) <sup>*</sup>	$v - >c$	$\Delta v$ (meV)	$\Delta c$ (meV)	$\Delta E_{B-A}$ (meV)	$I_A$ (pol.) ( $v -> c$ )	$I_B$ (pol.) ( $v-1 -> c+1$ )
$\text{FePS}_3$	Z-AFM	5.99 (0.27%)	K	0.9	6.4	7.3	0.34 (y)	0.37 (y)
	N-AFM	5.99 (0.31%)	+K	8.5	0.3	8.8	0.29 (x)/0.09 (z)	0.23 (x)/0.09 (z)
			-K	11.4	10	21.4	0.19 (y)	0.17 (y)

<sup>\*</sup>The  $\delta$  parameter denotes the deviation from the hexagonal symmetry as defined in Equation 2.

**Figure 5(a)** portrays a scheme of band-edge states in a benchmark material, the  $\text{MnPS}_3$ , as a reference to that of  $\text{FePS}_3$ , characterized by isotropic hexagons, with a presence of *Neél*-AFM magnetic arrangement. The calculation exposes non-degenerate double valleys ( $K^+$  and  $K^-$ ) due to the influence of the *Neél* sub-magnetic fields, while each valley has a spin degeneracy (red and black curves and arrows). The optical transitions are marked by double-arrows with polarization along the *z*-axis (a normal to the honeycomb plane). The color codes and notations as in panel (a) are kept in the following panels.

**Figure 5(b)** displays a model in which Fe-atoms substitute for Mn-atoms, while preserving the lateral symmetric structure as in panel (a). Such a model leads to an electronic

structure with an indirect bandgap, when each band-edge has energy and spin degeneracy. Important to note, that due to the large contribution of the  $d$  states of Fe close to the Fermi level, the position of the band extrema depends on the Hubbard  $U$  parameter, and can be shifted from the  $K$  points as reported previously.<sup>39</sup> Inspection of the models described so far, exposes a conflict with the experimental observations. Mainly, a lack in the removal of energy and spin degeneracy of the band-edge transitions, and the exceptionally sharp and intense LE transition. Hence, additional consideration is required, specifically to the existence of anisotropy in the lateral dimensions, resulting in *local inversion symmetry breaking*, as exposed through the XRD observations above. Thus, implementing DFT+U+SOC in combination with the mentioned lateral anisotropy led to the following two models, which at a certain temperature can be energetically compatible.

**Figure 5(c)** displays the band-edge electronic states of the  $\text{FePS}_3$  *zigzag*-AFM structure, showing a single valley, albeit comprised of split bright electronic states, each with unitary spin polarization. The split energies in the conduction and valence bands are labeled as  $\Delta_c$  and  $\Delta_v$ , while the states in energetic ascending order are indicated as  $v-1$ ,  $v$ ,  $c$ , and  $c+1$  (see **Table 3**). The inter-band transitions (A and B) are polarized along the  $y$ -axis. This model is compatible with the experimental results, showing circular polarization in the  $a/b$  plane and a large transition probability (with units  $(\text{eV} \cdot \text{A})^2$  and labels  $I_{A,B}$  in **Table 3**) that supports the appearance of an intense and sharp LE band. Note that experimentally, the emission and excitation are along a normal to the sample slab; however, the light E-vector lies on the  $a/b$  plane, hence, sensing the lateral polarization. The energy gaps ( $\Delta_c, v$ ) were evaluated to be 7-8 meV (**Table 3**), close to the experimental energetic gap between LE1 and LE2 as shown in **Figure 3(b)**, while both are circularly polarized. So, the unique phenomena associated with the LE band originate from a structural anisotropy, rather than a *zigzag* directionality as previously proposed by Zhang et. al.<sup>21</sup>

**Figure 5(d)** disputes an additional alternative for a situation similar to that in panel (c), however, the magnetic structure is *Neél*-AFM. Such a situation is characterized by non-degenerate double valleys at  $K+$  and  $K-$  points (with breakage of inversion and time-reversal symmetry),<sup>46</sup> when the energy difference between the inter-band gaps ( $\Delta E_{BA}$ ) is also around 7 meV, although the polarization is along the  $x/z$ -axis. This cannot be excluded since indeed the polarization within the  $a/b$  plane had been reduced (see **Figure 5**), on the account of a flip of the spin orientation to the  $z$ -direction above  $\sim 40\text{K}$  as was shown in **Figure 3(c)**. This is related to a co-existence of the scenarios described in panels (c) and (d). A mixture of phases was defined here as a metastable regime, which is commensurate with the spin-exchange interaction calculations. Comparison between the models shown in panels (c) and (d) unprecedently express a dependence of the electronic band structure on the magnetic arrangement. Moreover, the intensity of the  $A^+$  peak is smaller than that of  $B^+$  peak in comparison to the corresponding intensities of the AFM- $z$  phase. Hence, the decrease of LE-1 intensity and increase of LE-2 intensity above 40K shown in **Figure 3(c)** may be attributed to a contribution of the N-AFM phase. For the model in Figure 5(d) to match our case, two additional peaks should be observable in the optical measurements;  $A^-$  and  $B^-$  (for  $-K$  valley). They should appear around 70 meV above the LE-1 peak, with a 20 meV spacing between them, with a smaller intensity than LE-1, according to DFT+U calculations. Hence, we conclude that the model shown in **Figure 5(c)** fits best with our experimental results, as we do not observe such transitions. This

proves that we observe a single valley with split bright electronic states with spin polarization of opposing spin directions.

### 3. Conclusion

The current study revealed for the first time, a strong impact of the lateral crystal distortion on the magnetic arrangement, and on the optical properties of FePS<sub>3</sub> single crystal, based on the correlation between magneto-photoluminescence (MPL) and XRD measurements at low temperatures. The XRD measurements uncovered an anisotropy in the a/b crystallographic plane, which causes inversion symmetry breaking and hence changes in the electronic and optical transitions of the compound. Moreover, circular polarized band-edge recombination emission and linearly polarized at the off-band-edge region reflected distinct selection rules which emanated from the induced changes in the electronic properties. Furthermore, temperature-dependent MPL measurements reflected zigzag-AFM at low temperatures and the coexistence of zigzag or Neél at mid temperatures. Theoretical calculations implementing anisotropy in spin-exchange interactions among Fe atom's NNs were evaluated by a modified Heisenberg Hamiltonian, which disclosed a stable zigzag arrangement that is tilted away from the a-axis. The direction of zigzag arrangement was further confirmed by linear dichroism of the off-band-edge transition. DFT calculations of the electronic band-edge predicted split states in degenerate symmetric points (K+/K-) for zigzag structure and non-degenerate for the Neél arrangement. Both cases required the inclusion of a crystallographic anisotropy parameter for the simulation of the experimental observations and showed band-edge selection rules with circularly polarized transitions, hence, strongly supporting the experimental observations close to the band-edge spectral regime. Overall, the study showed a strong correlation between the structural anisotropy in FePS<sub>3</sub> and the magnetic and optical properties of the material.

### 4. Methods

#### *Sample preparation:*

FePS<sub>3</sub> bulk crystals were synthesized via a chemical vapor transport (CVT) synthesis method described in our previous work.<sup>39</sup> The iron, red phosphorus, and sulfur in the ratio (1:1:3) were sealed inside an evacuated quartz ampoule with pressure below  $3.5 \times 10^{-5}$  Torr. A 5% molar excess of sulfur was added as a transporting agent to increase the chemical yield. The ampoule was placed in a two-zone furnace where the substrate zone was kept to 850°C and the deposition zone at 790°C for 7 days.

#### *Optical and Magneto-Optical spectroscopy:*

Temperature-dependent- and magneto-photoluminescence (T-PL, MPL) spectra were measured by mounting a bulk FePS<sub>3</sub> flake on a Si substrate into a fiber-based confocal microscope. The microscope was embedded into a cryogenic system (attoDRY1000 closed cycle cryostat). The microscope included an objective lens with an NA of 0.65 and a 473nm long-pass dichroic mirror. A ceramic heater on the sample stage allowed for T-PL spectra to be recorded, where the temperature of the sample was increased gradually from 4K-290K. A magnet within the cryostat system enabled MPL spectra to be recorded where the external magnetic field was varied from 0T-7T and -7T. Circular polarized MPL spectra were recorded using a suitable linear polarizer and  $\lambda/4$  waveplate in line with the emitted light from the

sample. Linear polarized MPL spectra were recorded by placing a linear polarizer in the excitation and emission line of the confocal microscope, which were rotated from 0°-360°. The target sample was excited using a continuous wave 405nm laser diode, where the emission from the sample was detected using a FERGIE spectrograph. XYZ piezo-electric positioners allowed to focus the laser beam on a desired spot on the sample. MPL and T-PL spectra were recorded under an illumination power of 0.3 mW.

**Computational Details:**

Inversion symmetry breaking: We quantify the degree of inversion symmetry breaking by the  $\Delta_{a,b,c}$  parameter, as presented by equation 5:

$$\begin{aligned}\Delta_a &= (\text{mean}(MS1, MS2) - \text{mean}(MS4, MS5)) / \text{mean}(MS1 - 6) \\ \Delta_b &= (\text{mean}(MS1, MS5) - \text{mean}(MS2, MS4)) / \text{mean}(MS1 - 6) \\ \Delta_c &= (MS6 - MS3) / \text{mean}(MS1 - 6)\end{aligned}\quad (5)$$

A perfect octahedron with equal MS bond lengths will compute to be  $\Delta_{a,b,c} = 0$  where any deviation from it results in inversion symmetry breaking. The  $\Delta_{a,b,c}$  parameters are a projected quantity over the  $a$ ,  $b$ , and  $c$  crystallographic axis, respectively. Therefore, the inversion offset can be defined as the magnitude of  $\|[\Delta_a, \Delta_b, \Delta_c]\|$ . However, we find that  $\Delta_a$  and  $\Delta_c$  are negligible compared to  $\Delta_b$ , hence we focus only on the  $\Delta_b$  parameter.

Exchange couplings: The calculations were carried out using the density functional theory (DFT) applying the Perdew–Burke–Ernzerhof (PBE) generalized gradient approximation to express the exchange-correlation functional<sup>47</sup> using the projector augmented wave (PAW) pseudopotentials, as implemented in the open-source DFT, package Quantum Espresso.<sup>48</sup> All calculations were carried out with a plane-wave basis using a kinetic energy cut-off of 80 and 90 Ry for FePS<sub>3</sub> and MnPS<sub>3</sub>, respectively. To account for the  $d$ -orbital localization, we incorporate the Hubbard potential (DFT+U), setting  $U$  as 3eV for 3d open shells of Mn and Fe atoms.<sup>49</sup> For structural optimization, we used ion relaxation posterior to a minimized Birch–Murnaghan plot, keeping the  $a/b$  lattice parameters ratio constant. This approach should account for full structural optimization of the MPX<sub>3</sub> monolayers while maintaining the crystal's symmetry.

The exchange interaction variables of anisotropic FePS<sub>3</sub> were extracted using DFT+U, starting from crystallographic coordinates taken from a single crystal XRD measurement at 140K. To extract the  $J$ -coefficients, all calculations were spin-polarized and were set to 7 magnetic supercell configurations, all of which are shown in figure 6. Using the DFT energies of these magnetic configurations, we were able to extract a set of six linear, independent equations to calculate all of the anisotropic exchange parameters in FePS<sub>3</sub> presented in equation 6:

$$\begin{aligned}J_{11} &= \frac{E_{FM} - E_{Neel} - E_{Stripe} + E_{Zigzag}}{8S^2} \\ J_{21} &= \frac{E_{FM} + E_{Neel} - E_{Stripe} - E_{Zigzag}}{16S^2}\end{aligned}$$

$$\begin{aligned}
J_{31} &= \frac{E_{FM} - E_{Neel} + E_{Stripe} - E_{ZigZag} + 2(E_{ab\,ZigZag} - 2E_{Striped\,ZigZag} + E_{ab\,Stripe})}{16S^2} \\
&\quad \frac{E_{FM} - E_{Neel} + E_{Stripe} - E_{ZigZag} + 2(E_{ab\,ZigZag} - E_{ab\,Striped})}{8S^2} \\
J_{22} &= \frac{E_{FM} + E_{Neel} + E_{Stripe} + E_{ZigZag} - 2(E_{ab\,ZigZag} + E_{ab\,Stripe})}{16S^2} \\
J_{32} &= \frac{E_{Striped\,ZigZag} - E_{ab\,ZigZag}}{2S^2}
\end{aligned} \tag{6}$$

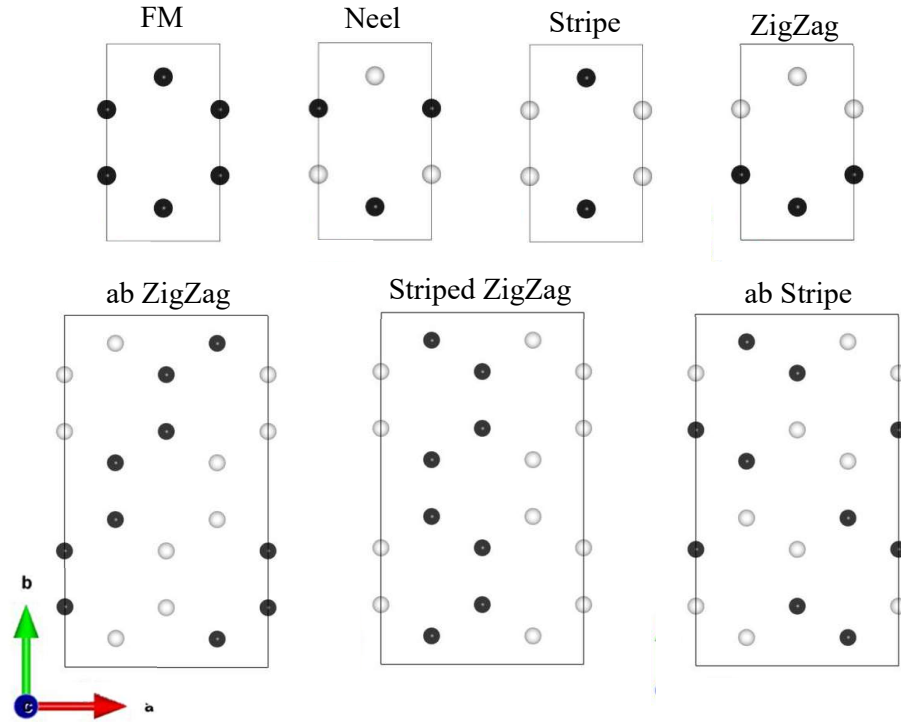


**Figure 6:** Seven magnetic supercell configurations. Black and white atoms refer to Fe in either a spin up or down states.

To validate our results, we tested our calculations against an isotropic  $FePS_3$  structure. For this case, the correct Heisenberg Hamiltonian collapses into tri-degenerate exchange interactions as described by equation 7:

$$\begin{aligned}
J_1 &= \frac{E_{FM} - E_{Neel} - E_{Stripe} + E_{ZigZag}}{8S^2} \\
J_2 &= \frac{E_{FM} + E_{Neel} - E_{Stripe} - E_{ZigZag}}{16S^2} \\
J_3 &= \frac{E_{FM} - E_{Neel} + 3E_{Stripe} - 3E_{ZigZag}}{24S^2}
\end{aligned} \tag{7}$$

***Electronic band structure:*** The calculation were performed within the PBE+U<sup>50</sup> and SOI included as implemented in the Vienna ab-initio simulation (VASP) package.<sup>51</sup> For both monolayers, we adopted the Hubbard U parameters equal to U=5.3 for FePS<sub>3</sub><sup>39</sup> and U=5 for MnPS<sub>3</sub>. The lattice and the position of the atoms have been fully optimized within the DFT+U and SOI included. The plane wave basis set with an energy cutoff equal to 500 eV was employed, whereas the  $k$ -points in the Brillouin zone were sampled on a 20x12x2 grid. The dispersive forces have been included in the framework of a semi-empirical Grimme method with a D3 parametrization (DFT-D3).<sup>52</sup> The selection rules have been obtained by calculating the direct interband momentum matrix elements between the band edges, namely, the valence band maximum (v) and conduction band minimum (c) at  $\mathbf{k}$  point ( $\mathbf{p}_{cv\mathbf{k}}$ ) using the density functional perturbation theory.<sup>53</sup> The optically allowed transition are determined by dipole selection rules:  $|x \mathbf{p}_{cv\mathbf{k}}|^2 > 0 \leftrightarrow x$ ;  $|y \mathbf{p}_{cv\mathbf{k}}|^2 > 0 \leftrightarrow y$ ;  $|z \mathbf{p}_{cv\mathbf{k}}|^2 > 0 \leftrightarrow z$ ,  $|e_+ \mathbf{p}_{cv\mathbf{k}}|^2 > 0 \leftrightarrow \sigma^+$ ,  $|e_- \mathbf{p}_{cv\mathbf{k}}|^2 > 0 \leftrightarrow \sigma^-$ , where  $x = [1,0,0]$ ,  $y = [0,1,0]$ ,  $z = [0,0,1]$ ,  $e_{\pm} = [1, \pm i, 0]/\sqrt{2}$ . Here, we describe in detail the structural models employed in band structure calculations: model (a) relaxed structure (lattice parameters and position of the atoms are optimized within DFT+U approach) for magnetic groundstate of MnPS<sub>3</sub> (AFM-N); model (b) relaxed structure taken from MnPS<sub>3</sub> and assumed for magnetic groundstate of FePS<sub>3</sub> (AFM-z); model (c) the optimized lattice parameters and position of the atoms for magnetic groundstate of FePS<sub>3</sub>; model (d) the optimized lattice parameters and position of the atoms for FePS<sub>3</sub> assuming the AFM-Neel type of magnetic order. Note, that the AFM-z is lower in energy than AFM-N magnetic phase, by about a few up to tens of meV per magnetic ion, depending on the Hubbard U parameter.

## Supporting Information

Supporting Information is available from the Wiley Online Library or the author. It includes the original EDX and XRD data, Gaussian fits, and surplus magneto-PL observations.

## Acknowledgments

This work was supported by the Deutsch – Israel Program (DIP, project no.NA1223/2-1), the Israel Science Foundation (ISF, project no. 2528/19) and the Binational Science Foundation – NSF (Project 2017/637). A. K. B. and E. L. were supported by the European Commission via the Marie Skłodowska-Curie action Phonsi (H2020-MSCA-ITN-642656). M.B. acknowledges support by the University of Warsaw within the project “Excellence Initiative-Research University” programme. Access to computing facilities of PL-Grid Polish Infrastructure for Supporting Computational Science in the European Research Space and of the Interdisciplinary Center of Modeling (ICM), University of Warsaw are gratefully acknowledged. We thank Dr. Natalia Friedman (Technion, Israel) for carrying the single-crystal XRD measurements, and Dr. Olga Kleinerman (Technion, Israel) for assistance with SEM and EDX measurements.

## References

- (1) Zhang, Y.; Xu, H.; Feng, J.; Wu, H.; Yu, G.; Han, X. Magnetic Two-Dimensional van Der Waals Materials for Spintronic Devices. *Chinese Physics B*. 2022.
- (2) Liang, S. J.; Cheng, B.; Cui, X.; Miao, F. Van Der Waals Heterostructures for High-Performance Device Applications: Challenges and Opportunities. *Advanced Materials*. 2020.
- (3) Huang, B.; Clark, G.; Navarro-Moratalla, E.; Klein, D. R.; Cheng, R.; Seyler, K. L.; Zhong, Di.; Schmidgall, E.; McGuire, M. A.; Cobden, D. H.; Yao, W.; Xiao, D.; Jarillo-Herrero, P.; Xu, X. Layer-Dependent Ferromagnetism in a van Der Waals Crystal down to the Monolayer Limit. *Nature* **2017**, *546*, 270–273.
- (4) Fang, Y.; Wu, S.; Zhu, Z.-Z.; Guo, G.-Y. Large Magneto-Optical Effects and Magnetic Anisotropy Energy in Two-Dimensional Cr<sub>2</sub>Ge<sub>2</sub>Te<sub>6</sub>. *Phys. Rev. B* **2018**, *98*, 125416.
- (5) Wu, Y.; Zhang, S.; Zhang, J.; Wang, W.; Zhu, Y. L.; Hu, J.; Yin, G.; Wong, K.; Fang, C.; Wan, C.; Han, X.; Shao, Q.; Taniguchi, T.; Watanabe, K.; Zang, J.; Mao, Z.; Zhang, X.; Wang, K. L. Néel-Type Skyrmion in WTe<sub>2</sub>/Fe<sub>3</sub>GeTe<sub>2</sub> van Der Waals Heterostructure. *Nat. Commun.* **2020**, *11*.
- (6) Wang, F.; Shifa, T. A.; Yu, P.; He, P.; Liu, Y.; Wang, F.; Wang, Z.; Zhan, X.; Lou, X.; Xia, F.; He, J. New Frontiers on van Der Waals Layered Metal Phosphorous Trichalcogenides. *Adv. Funct. Mater.* **2018**, *28*, 1802151.
- (7) Susner, M. A.; Chyasnichiyus, M.; McGuire, M. A.; Ganesh, P.; Maksymovych, P. Metal Thio- and Selenophosphates as Multifunctional van Der Waals Layered Materials. *Adv. Mater.* **2017**, *29*, 1602852.
- (8) Chittari, B. L.; Park, Y.; Lee, D.; Han, M.; Macdonald, A. H.; Hwang, E.; Jung, J. Electronic and Magnetic Properties of Single-Layer M PX3 Metal Phosphorous Trichalcogenides. *Phys. Rev. B* **2016**, *94*, 184428.
- (9) Li, H.; Ruan, S.; Zeng, Y. Intrinsic Van Der Waals Magnetic Materials from Bulk to the 2D Limit: New Frontiers of Spintronics. *Adv. Mater.* **2019**, *31*, 1900065.
- (10) Kuo, C. T.; Neumann, M.; Balamurugan, K.; Park, H. J.; Kang, S.; Shiu, H. W.; Kang, J. H.; Hong, B. H.; Han, M.; Noh, T. W.; Park, J. G. Exfoliation and Raman Spectroscopic Fingerprint of Few-Layer NiPS<sub>3</sub> Van Der Waals Crystals. *Sci. Rep.* **2016**, *6*, 20904.
- (11) Liu, J.; Li, X.-B.; Wang, D.; Lau, W.-M.; Peng, P.; Liu, L.-M. Diverse and Tunable Electronic Structures of Single-Layer Metal Phosphorus Trichalcogenides for Photocatalytic Water Splitting. *J. Chem. Phys.* **2014**, *140*, 054707.
- (12) Mermin, N. D.; Wagner, H. Absence of Ferromagnetism or Antiferromagnetism in One- or Two-Dimensional Isotropic Heisenberg Models. *Phys. Rev. Lett.* **1966**, *17*, 1133–1136.
- (13) Hohenberg, P. C. Existence of Long-Range Order in One and Two Dimensions. *Phys. Rev.* **1967**, *158*, 383–386.
- (14) Mayorga-Martinez, C. C.; Sofer, Z.; Sedmidubský, D.; Huber, Š.; Eng, A. Y. S.;

Pumera, M. Layered Metal Thiophosphite Materials: Magnetic, Electrochemical, and Electronic Properties. *ACS Appl. Mater. Interfaces* **2017**, *9*, 12563–12573.

(15) Cortie, D. L.; Causer, G. L.; Rule, K. C.; Fritzsch, H.; Kreuzpaintner, W.; Klose, F. Two-Dimensional Magnets: Forgotten History and Recent Progress towards Spintronic Applications. *Adv. Funct. Mater.* **2020**, *30*, 1901414.

(16) Gong, C.; Zhang, X. Two-Dimensional Magnetic Crystals and Emergent Heterostructure Devices. *Science (80-.)* **2019**, *363*, 4450.

(17) Xing, W.; Qiu, L.; Wang, X.; Yao, Y.; Ma, Y.; Cai, R.; Jia, S.; Xie, X. C.; Han, W. Magnon Transport in Quasi-Two-Dimensional van Der Waals Antiferromagnets. *Phys. Rev. X* **2019**, *9*, 011026.

(18) Ur Rehman, Z.; Muhammad, Z.; Moses, O. A.; Zhu, W.; Wu, C.; He, Q.; Habib, M.; Song, L. Magnetic Isotropy/Anisotropy in Layered Metal Phosphorous Trichalcogenide MPS3 (M = Mn, Fe)Single Crystals. *Micromachines* **2018**, *9*.

(19) Long, G.; Henck, H.; Gibertini, M.; Dumcenco, D.; Wang, Z.; Taniguchi, T.; Watanabe, K.; Giannini, E.; Morpurgo, A. F. Persistence of Magnetism in Atomically Thin MnPS3 Crystals. *Nano Lett.* **2020**.

(20) Sivadas, N.; Daniels, M. W.; Swendsen, R. H.; Okamoto, S.; Xiao, D. Magnetic Ground State of Semiconducting Transition-Metal Trichalcogenide Monolayers. *Phys. Rev. B - Condens. Matter Mater. Phys.* **2015**, *91*, 1–6.

(21) Zhang, Q.; Hwangbo, K.; Wang, C.; Jiang, Q.; Chu, J.-H.; Wen, H.; Xiao, D.; Xu, X. Observation of Giant Optical Linear Dichroism in a Zigzag Antiferromagnet FePS3. *Nano Lett.* **2021**, *21*, 6938–6945.

(22) Zhang, J.; Nie, Y.; Wang, X.; Xia, Q.; Guo, G. Strain Modulation of Magnetic Properties of Monolayer and Bilayer FePS3 Antiferromagnet. *J. Magn. Magn. Mater.* **2021**, *525*, 167687.

(23) Lee, J. U.; Lee, S.; Ryoo, J. H.; Kang, S.; Kim, T. Y.; Kim, P.; Park, C. H.; Park, J. G.; Cheong, H. Ising-Type Magnetic Ordering in Atomically Thin FePS3. *Nano Lett.* **2016**, *16*, 7433–7438.

(24) Wang, X.; Du, K.; Fredrik Liu, Y. Y.; Hu, P.; Zhang, J.; Zhang, Q.; Owen, M. H. S.; Lu, X.; Gan, C. K.; Sengupta, P.; Kloc, C.; Xiong, Q. Raman Spectroscopy of Atomically Thin Two-Dimensional Magnetic Iron Phosphorus Trisulfide (FePS 3 ) Crystals. *2D Mater.* **2016**, *3*, 031009.

(25) Kang, S.; Kim, K.; Kim, B. H.; Kim, J.; Sim, K. I.; Lee, J.-U.; Lee, S.; Park, K.; Yun, S.; Kim, T.; Nag, A.; Walters, A.; Garcia-Fernandez, M.; Li, J.; Chapon, L.; Zhou, K.-J.; Son, Y.-W.; Kim, J. H.; Cheong, H.; Park, J.-G. Coherent Many-Body Exciton in van Der Waals Antiferromagnet NiPS3. *Nature* **2020**, *583*, 785–789.

(26) Kim, S. Y.; Kim, T. Y.; Sandilands, L. J.; Sinn, S.; Lee, M.-C.; Son, J.; Lee, S.; Choi, K.-Y.; Kim, W.; Park, B.-G.; Jeon, C.; Kim, H.-D.; Park, C.-H.; Park, J.-G.; Moon, S. J.; Noh, T. W. Charge-Spin Correlation in van Der Waals Antiferromagenet NiPS3. *Phys. Rev. Lett.* **2017**, *120*, 136402.

(27) Brec, R. Review on Structural and Chemical Properties of Transition Metal Phosphorous Trisulfides MPS3. *Solid State Ionics* **1986**, *22*, 3–30.

(28) Kurosawa, K.; Saito, S.; Yamaguchi, Y. Neutron Diffraction Study on MnPS3 and

FePS3. *J. Phys. Soc. Japan* **1983**, *52*, 3919–3926.

(29) Wiedenmann, A.; Rossat-Mignod, J.; Louisy, A.; Brec, R.; Rouxel, J. Neutron Diffraction Study of the Layered Compounds MnPSe<sub>3</sub> and FePSe<sub>3</sub>. *Solid State Commun.* **1981**, *40*, 1067–1072.

(30) Li, X.; Wu, X.; Yang, J. Half-Metallicity in MnPSe<sub>3</sub> Exfoliated Nanosheet with Carrier Doping. *J. Am. Chem. Soc.* **2014**, *136*, 11065–11069.

(31) Joy, P. A.; Vasudevan, S. Magnetism in the Layered Transition-Metal Thiophosphates MPS<sub>3</sub> (M=Mn, Fe, and Ni). *Phys. Rev. B* **1992**, *46*, 5425–5433.

(32) Lançon, D.; Walker, H. C.; Ressouche, E.; Ouladdiaf, B.; Rule, K. C.; McIntyre, G. J.; Hicks, T. J.; Rønnow, H. M.; Wildes, A. R. Magnetic Structure and Magnon Dynamics of the Quasi-Two-Dimensional Antiferromagnet FePS<sub>3</sub>. *Phys. Rev. B* **2016**, *94*, 214407.

(33) Rule, K. C.; McIntyre, G. J.; Kennedy, S. J.; Hicks, T. J. Single-Crystal and Powder Neutron Diffraction Experiments on FePS<sub>3</sub>. *Phys. Rev. B* **2007**, *76*, 134402.

(34) Wildes, A. R.; Lançon, D.; Chan, M. K.; Weickert, F.; Harrison, N.; Simonet, V.; Zhitomirsky, M. E.; Gvozdikova, M. V.; Ziman, T.; Rønnow, H. M. High Field Magnetization of FePS<sub>3</sub>. *Phys. Rev. B* **2020**.

(35) Murayama, C.; Okabe, M.; Urushihara, D.; Asaka, T.; Fukuda, K.; Isobe, M.; Yamamoto, K.; Matsushita, Y. Crystallographic Features Related to a van Der Waals Coupling in the Layered Chalcogenide FePS<sub>3</sub>. *J. Appl. Phys.* **2016**, *120*, 142114.

(36) Zhang, J. min; Nie, Y. zhuang; Wang, X. guang; Xia, Q. lin; Guo, G. hua. Strain Modulation of Magnetic Properties of Monolayer and Bilayer FePS<sub>3</sub> Antiferromagnet. *J. Magn. Magn. Mater.* **2021**, *525*, 167687.

(37) Koo, H.-J.; Kremer, R.; Whangbo, M.-H. Unusual Spin Exchanges Mediated by the Molecular Anion P2S<sub>6</sub>–: Theoretical Analyses of the Magnetic Ground States, Magnetic Anisotropy and Spin Exchanges of MPS<sub>3</sub> (M = Mn, Fe, Co, Ni). *Molecules* **2021**, *26*, 1410.

(38) Nauman, M.; Kiem, D. H.; Lee, S.; Son, S.; Park, J. G.; Kang, W.; Han, M. J.; Jo, Y. Complete Mapping of Magnetic Anisotropy for Prototype Ising van Der Waals FePS<sub>3</sub>. *2D Mater.* **2021**, *8*.

(39) Budniak, A.; Zelewski, S.; Birowska, M.; Woźniak, T.; Bendikov, T.; Kauffmann, Y.; Amouyal, Y.; Kudrawiec, R.; Lifshitz, E. Spectroscopy and Structural Investigation of Iron Phosphorus Trisulfide—FePS<sub>3</sub>. *Adv. Opt. Mater.* **2022**.

(40) Hwangbo, K.; Zhang, Q.; Jiang, Q.; Wang, Y.; Fonseca, J.; Wang, C.; Diederich, G. M.; Gamelin, D. R.; Xiao, D.; Chu, J.-H.; Yao, W.; Xu, X. Highly Anisotropic Excitons and Multiple Phonon Bound States in a van Der Waals Antiferromagnetic Insulator. *Nat. Nanotechnol.* **2021**, *16*, 655–660.

(41) Lançon, D.; Walker, H. C.; Ressouche, E.; Ouladdiaf, B.; Rule, K. C.; McIntyre, G. J.; Hicks, T. J.; Rønnow, H. M.; Wildes, A. R. Magnetic Structure and Magnon Dynamics of the Quasi-Two-Dimensional Antiferromagnet  $\text{FePS}_3$ . *Phys. Rev. B* **2016**, *94*, 214407.

(42) Zhou, Y.; Duan, C.; Huang, Z.; - al; Wei, S.; Liao, X.; Wang, C.; Zhao, G.; Ke, X.; Li, X.; Wildes, A. R.; Rule, K. C.; Bewley, R. I.; Enderle, M.; Hicks, T. J. The Magnon

Dynamics and Spin Exchange Parameters of FePS3. *J. Phys. Condens. Matter* **2012**, *24*, 416004.

(43) Ghosh, A.; Birowska, M.; Ghose, P. K.; Rybak, M.; Maity, S.; Ghosh, S.; Das, B.; Bera, S.; Bhardwaj, S.; Nandi, S.; Datta, S. Anisotropic: Magnetodielectric Coupling in Layered Antiferromagnetic FePS3. **2022**.

(44) Batista, C. D.; Lin, S.-Z.; Hayami, S.; Azaria, P. Spin Waves in Frustrated Quantum Spin Systems. *J. Phys. C Solid State Phys.* **1986**, *19*, 2773.

(45) Zhang, X. X.; Li, L.; Weber, D.; Goldberger, J.; Mak, K. F.; Shan, J. Gate-Tunable Spin Waves in Antiferromagnetic Atomic Bilayers. *Nat. Mater.* *2020* **198** *2020*, *19*, 838–842.

(46) Li, X.; Cao, T.; Niu, Q.; Shi, J.; Feng, J. Coupling the Valley Degree of Freedom to Antiferromagnetic Order. *Proc. Natl. Acad. Sci. U. S. A.* **2013**, *110*, 3738–3742.

(47) Perdew, J. P.; Burke, K.; Ernzerhof, M. Generalized Gradient Approximation Made Simple. *Phys. Rev. Lett.* **1996**.

(48) Giannozzi, P.; Baroni, S.; Bonini, N.; Calandra, M.; Car, R.; Cavazzoni, C.; Ceresoli, D.; Chiarotti, G. L.; Cococcioni, M.; Dabo, I.; Dal Corso, A.; de Gironcoli, S.; Fabris, S.; Fratesi, G.; Gebauer, R.; Gerstmann, U.; Gouguassis, C.; Kokalj, A.; Lazzari, M.; Martin-Samos, L.; Marzari, N.; Mauri, F.; Mazzarello, R.; Paolini, S.; Pasquarello, A.; Paulatto, L.; Sbraccia, C.; Scandolo, S.; Sclauzero, G.; Seitsonen, A. P.; Smogunov, A.; Umari, P.; Wentzcovitch, R. M. QUANTUM ESPRESSO: A Modular and Open-Source Software Project for Quantum Simulations of Materials. *J. Phys. Condens. Matter* **2009**, *21*, 395502.

(49) Zhou, Y.; Duan, C.; Huang, Z.; - al; Wei, S.; Liao, X.; Wang, C.; Zhao, G.; Ke, X.; Li, X.; Olsen, T. Magnetic Anisotropy and Exchange Interactions of Two-Dimensional FePS3, NiPS3 and MnPS3 from First Principles Calculations. *J. Phys. D. Appl. Phys.* **2021**, *54*, 314001.

(50) Dudarev, S.; Botton, G. Electron-Energy-Loss Spectra and the Structural Stability of Nickel Oxide: An LSDA+U Study. *Phys. Rev. B - Condens. Matter Mater. Phys.* **1998**, *57*.

(51) Kresse, G.; Hafner, J. Ab Initio Molecular Dynamics for Liquid Metals. *Phys. Rev. B* **1993**, *47*.

(52) Grimme, S.; Antony, J.; Ehrlich, S.; Krieg, H. A Consistent and Accurate Ab Initio Parametrization of Density Functional Dispersion Correction (DFT-D) for the 94 Elements H-Pu. *J. Chem. Phys.* **2010**, *132*.

(53) Gajdoš, M.; Hummer, K.; Kresse, G.; Furthmüller, J.; Bechstedt, F. Linear Optical Properties in the Projector-Augmented Wave Methodology. *Phys. Rev. B - Condens. Matter Mater. Phys.* **2006**, *73*.

## Supporting Information

### Crystal anisotropy implications on the intrinsic magnetism in van der Waals FePS<sub>3</sub>

Ellenor Geraffy<sup>1#</sup>, Shahar Zuri<sup>1#</sup>, Milosz Marcin Rybak<sup>2</sup>, Faris Horani<sup>1</sup>, Adam K. Budniak<sup>1</sup>, Yaron Amouyal<sup>3</sup>, Magdalena Birowska<sup>\*2</sup> and Efrat Lifshitz<sup>\*1</sup>

<sup>1</sup>Schulich Faculty of Chemistry, Solid State Institute, Russell Berrie Nanotechnology Institute, and the Helen Diller Quantum Information Center, Technion – Israel Institute of Technology, 3200003 Haifa, Israel

<sup>2</sup>Institute of Theoretical Physics, Faculty of Physics, University of Warsaw, Pasteura 5, Warsaw 02-093, Poland

<sup>3</sup>Department of Materials Science and Engineering, Technion – Israel Institute of Technology, 3200003 Haifa, Israel

#Equal contribution

\*Corresponding authors

Email: [ssefrat@technion.ac.il](mailto:ssefrat@technion.ac.il) , [birowska@fuw.edu.pl](mailto:birowska@fuw.edu.pl)

#### 1. Characterization of single crystal FePS<sub>3</sub>

##### 1.1 EDX measurements

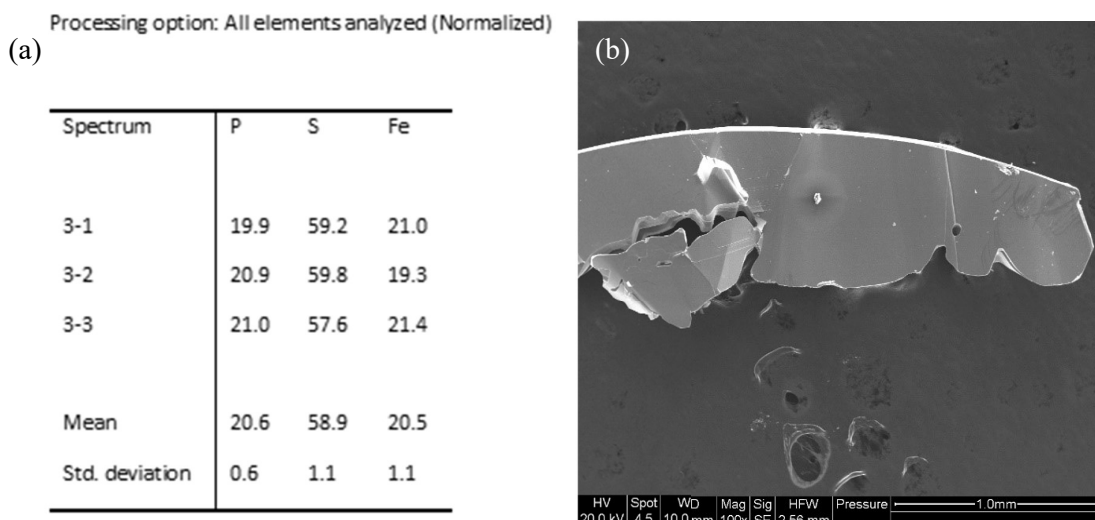


**Figure S1: EDX measurements of bulk FePS<sub>3</sub> synthesised via CVT. (a)** Percentage breakdown of each element in FePS<sub>3</sub> bulk sample, **(b)** SEM image of FePS<sub>3</sub> sample using the secondary electron (SE) detector.

## 1.2 XRD measurements

Table S 1 Bond lengths of bulk FePS<sub>3</sub> at 140K

Atom	Atom	Length/Å	Atom	Atom	Length/Å
Fe1	S1	2.5361(16)	S1	P1	2.0244(17)
Fe1	S1 <sup>1</sup>	2.5442(14)	S2	Fe1 <sup>4</sup>	2.5464(17)
Fe1	S1 <sup>2</sup>	2.5442(14)	S2	Fe1 <sup>6</sup>	2.5464(17)
Fe1	S1 <sup>3</sup>	2.5361(16)	S2	P1	2.031(3)
Fe1	S2 <sup>4</sup>	2.5464(17)	P1	S1 <sup>7</sup>	2.0244(17)
Fe1	S2 <sup>5</sup>	2.5464(17)	P1	P1 <sup>8</sup>	2.182(4)
S1	Fe1 <sup>1</sup>	2.5442(14)			

Table S 2 Bond angles of bulk FePS<sub>3</sub> at 140K

Atom	Atom	Atom	Angle/°	Atom	Atom	Atom	Angle/°
S1	Fe1	S1 <sup>1</sup>	94.91(7)	S2 <sup>4</sup>	Fe1	S2 <sup>5</sup>	94.85(7)
S1 <sup>1</sup>	Fe1	S1 <sup>2</sup>	95.51(5)	Fe1	S1	Fe1 <sup>3</sup>	84.49(5)
S1	Fe1	S1 <sup>2</sup>	85.13(5)	P1	S1	Fe1	103.14(8)
S1 <sup>1</sup>	Fe1	S1 <sup>3</sup>	85.13(5)	P1	S1	Fe1 <sup>3</sup>	103.23(8)
S1	Fe1	S1 <sup>3</sup>	95.51(5)	Fe1 <sup>4</sup>	S2	Fe1 <sup>6</sup>	85.15(7)
S1 <sup>2</sup>	Fe1	S1 <sup>3</sup>	179.05(8)	P1	S2	Fe1 <sup>6</sup>	103.24(8)
S1	Fe1	S2 <sup>4</sup>	179.57(5)	P1	S2	Fe1 <sup>4</sup>	103.24(8)
S1 <sup>1</sup>	Fe1	S2 <sup>5</sup>	179.57(5)	S1 <sup>7</sup>	P1	S1	114.41(12)
S1 <sup>1</sup>	Fe1	S2 <sup>4</sup>	85.12(5)	S1	P1	S2	114.05(7)
S1	Fe1	S2 <sup>5</sup>	85.12(5)	S1 <sup>7</sup>	P1	S2	114.05(7)
S1 <sup>2</sup>	Fe1	S2 <sup>4</sup>	94.44(6)	S1 <sup>7</sup>	P1	P1 <sup>8</sup>	104.39(8)
S1 <sup>3</sup>	Fe1	S2 <sup>4</sup>	84.91(6)	S1	P1	P1 <sup>8</sup>	104.39(8)
S1 <sup>2</sup>	Fe1	S2 <sup>5</sup>	84.91(6)	S2	P1	P1 <sup>8</sup>	103.88(14)
S1 <sup>3</sup>	Fe1	S2 <sup>5</sup>	94.44(6)				

Table S 3 Bond lengths of bulk FePS<sub>3</sub> at RT

Atom	Atom	Length/Å	Atom	Atom	Length/Å
Fe1	S1	2.539(3)	S1	P1	2.030(3)
Fe1	S1 <sup>1</sup>	2.547(3)	S2	Fe1 <sup>4</sup>	2.549(3)
Fe1	S1 <sup>2</sup>	2.547(3)	S2	Fe1 <sup>6</sup>	2.549(3)
Fe1	S1 <sup>3</sup>	2.539(3)	S2	P1	2.027(4)
Fe1	S2 <sup>4</sup>	2.550(3)	P1	S1 <sup>7</sup>	2.030(3)
Fe1	S2 <sup>5</sup>	2.549(3)	P1	P1 <sup>8</sup>	2.191(6)
S1	Fe1 <sup>1</sup>	2.547(3)			

Table S 4: Bond angles of bulk FePS<sub>3</sub> at RT

Atom	Atom	Atom	Angle/°	Atom	Atom	Atom	Angle/°
S1	Fe1	S1 <sup>1</sup>	94.84(13)	S2 <sup>4</sup>	Fe1	S2 <sup>5</sup>	94.61(14)
S1 <sup>1</sup>	Fe1	S1 <sup>2</sup>	95.57(11)	Fe1	S1	Fe1 <sup>3</sup>	84.43(11)

<b>S1</b>	Fe1	S1 <sup>2</sup>	85.09(11)	P1	S1	Fe1	103.25(14)
<b>S1<sup>1</sup></b>	Fe1	S1 <sup>3</sup>	85.09(11)	P1	S1	Fe1 <sup>3</sup>	103.34(11)
<b>S1</b>	Fe1	S1 <sup>3</sup>	95.57(11)	Fe1 <sup>4</sup>	S2	Fe1 <sup>6</sup>	85.39(14)
<b>S1<sup>2</sup></b>	Fe1	S1 <sup>3</sup>	179.03(10)	P1	S2	Fe1 <sup>6</sup>	103.29(13)
<b>S1</b>	Fe1	S2 <sup>4</sup>	179.53(7)	P1	S2	Fe1 <sup>4</sup>	103.29(13)
<b>S1<sup>1</sup></b>	Fe1	S2 <sup>5</sup>	179.53(7)	S1 <sup>7</sup>	P1	S1	114.46(18)
<b>S1<sup>1</sup></b>	Fe1	S2 <sup>4</sup>	85.28(12)	S1	P1	P1 <sup>8</sup>	104.15(10)
<b>S1</b>	Fe1	S2 <sup>5</sup>	85.28(12)	S1 <sup>7</sup>	P1	P1 <sup>8</sup>	104.15(10)
<b>S1<sup>2</sup></b>	Fe1	S2 <sup>4</sup>	94.44(11)	S2	P1	S1 <sup>7</sup>	114.15(11)
<b>S1<sup>3</sup></b>	Fe1	S2 <sup>4</sup>	84.90(11)	S2	P1	S1	114.16(11)
<b>S1<sup>2</sup></b>	Fe1	S2 <sup>5</sup>	84.90(11)	S2	P1	P1 <sup>8</sup>	104.04(18)
<b>S1<sup>3</sup></b>	Fe1	S2 <sup>5</sup>	94.44(11)				

## 2. DFT+U calculations

**Table S5** :DFT +U calculated energies for FePS<sub>3</sub>, assuming the lattice parameters and positions of the atoms taken from XRD measurements

	Energy [Ry/cell]	Energy [eV/cell]	Energy [eV/atom]	dE [meV/atom]	Thermal energy [K]
FM	- 1322.780079	- 17997.34637	-899.867	89.09	<b>1033.89</b>
Neél	- 1322.910919	- 17999.12653	-899.956	0.08	<b>0.96</b>
Zigzag	- 1322.781094	- 17997.36017	-899.868	88.40	<b>1025.89</b>
Stripe	- 1322.833431	- 17998.07225	-899.903	52.79	<b>612.70</b>
a/b Zigzag	- 1322.911041	- 17999.12819	-899.956	0	<b>0</b>
Striped Zigzag	- 1322.907365	- 17999.07817	-899.953	2.50	<b>29.01</b>
a/b Stripe	- 1322.907107	- 17999.07466	-899.953	2.67	<b>31.05</b>

**Table S6** : DFT+U calculated energies for MnPS<sub>3</sub>

	Energy [Ry/cell]	Energy [eV/cell]	Energy [eV/atom]	dE [meV/atom]	Thermal energy [K]
FM	- 1322.85805	-17998.40721	-899.9203607	36.24	<b>420.66</b>
Neél	- 1322.91133 5	-17999.13219	-899.9566093	0	<b>0</b>
Zigzag	- 1322.90251 2	-17999.01215	-899.9506073	6.00	<b>69.653</b>

Stripe	-	-17999.13317	-899.9566583	-0.04	<b>-0.56</b>
	1322.91140 7				

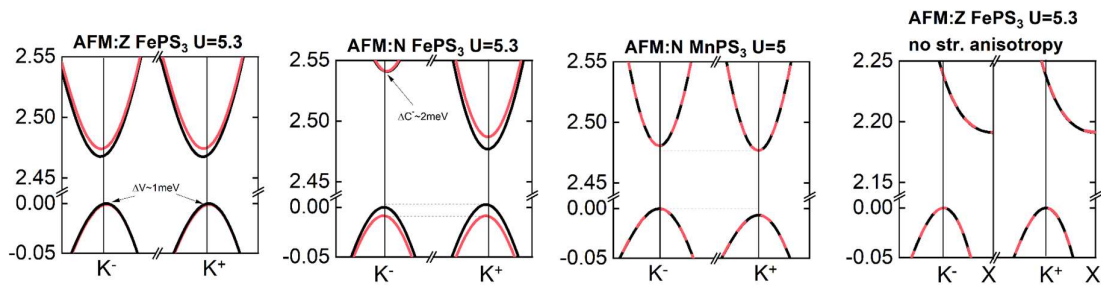


**Figure S 2: Band structures in vicinity of Fermi level: using DFT+U+SOI (U=5.3eV for FePS3, U=5eV for MnPS<sub>3</sub>)**

### 3. Optical Measurements

#### 3.1 ME transition measurements

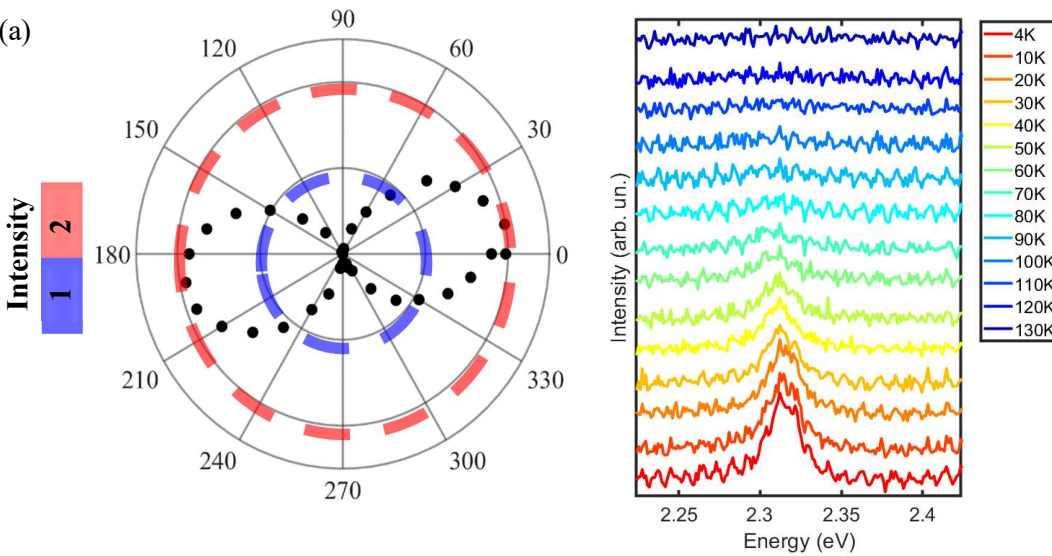


**Figure S 3: Optical measurements of ME transition. (a) Polar plot of linear polarization measurements of ME transition at 4K. (b) Temperature dependent measurements of ME transition, where T = 4-130K**

### 3.2 Gaussian fits of PL spectra

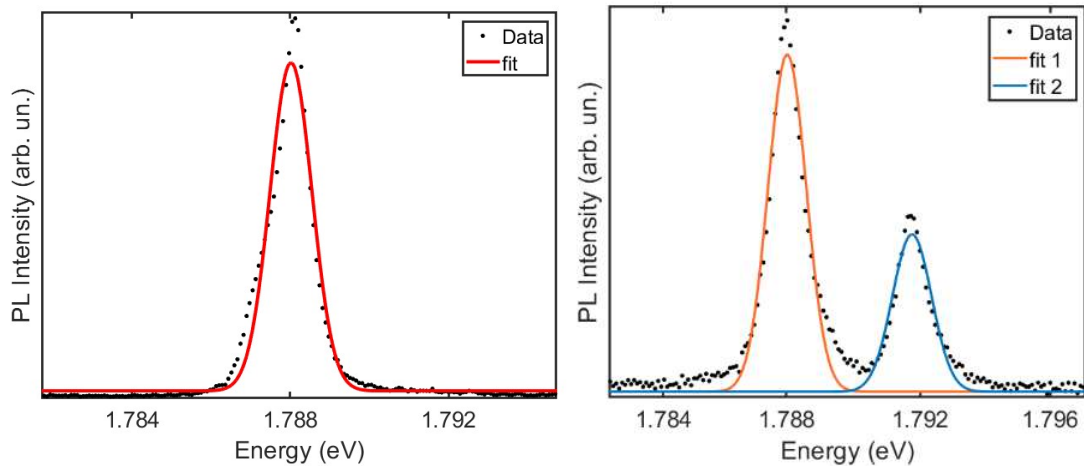


Figure S 4: Gaussian fits of LE transition at (a) 4K and (b) 70K.

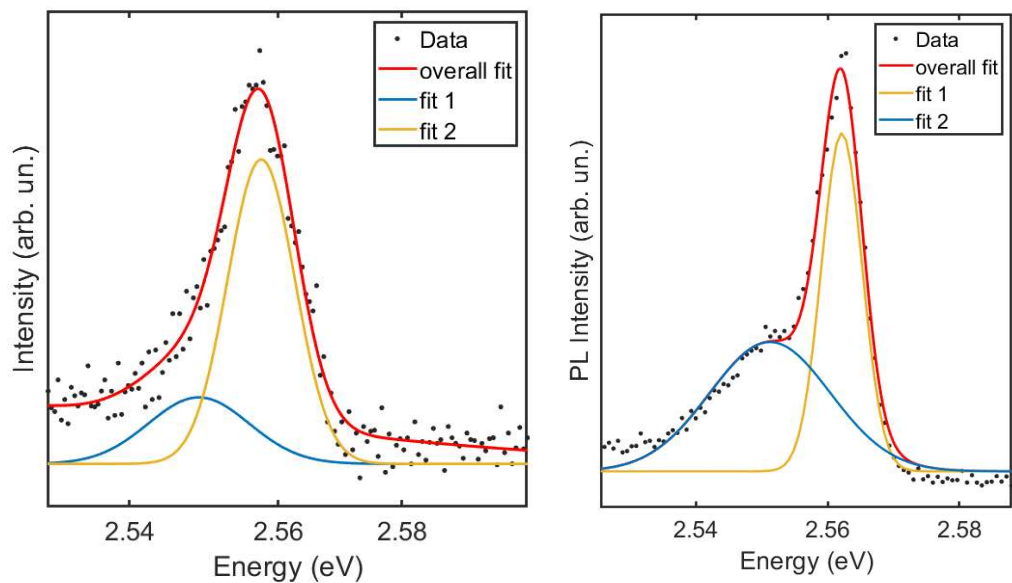


Figure S 5: Gaussian fits of HE transition at (a) 4K and (b) 70K